EVALUATION OF SPEED EFFECT ON DYNAMIC STALL BASED ON LOW AND HIGH FIDELITY AEROELASTIC ROTOR SIMULATIONS

François Richez, ONERA/DAAA/Institut Polytechnique de Paris, Meudon, France
Ilyès Berhouni, ONERA/DAAA/Institut Polytechnique de Paris, Meudon, France
Joëlle Bailly, ONERA/DAAA/Institut Polytechnique de Paris, Meudon, France

Abstract

This paper aims at analyzing the effects of an increasing advance ratio on the stall characteristics of a helicopter rotor in forward flight. This numerical investigation is performed with both a low fidelity approach based on free wake model and a high fidelity approach based on CFD. The objective is twofold: first, evaluate the capability of the free wake approach in predicting stall, and second, describe the flow characteristics specific to stall at high advance ratio. The results show that the low fidelity approach correctly predicts the global trend of dynamic stall at both moderate ($\mu = 0.35$) and high advance ratio ($\mu = 0.55$), but underestimates the intensity of the airloads fluctuations induced by stall. An in-depth analysis of high fidelity results has highlighted the main phenomena associated with stall at moderate and high speeds, and in particular the important role played by wake dynamics.

1. NOTATION

Symbols

A	Rotor area, πR^2, m²
b	Blade number
c	Blade chord length, m
C_P/σ	Rotor power coefficient, $M_z/[\rho_\infty A\sigma R(R\Omega)^2]$
C_T/σ	Rotor lift coefficient, $F_z/[\rho_\infty A\sigma(R\Omega)^2]$
C_X/σ	Rotor propulsive coefficient, (negative when dragging), $F_x/[\rho_\infty A\sigma(R\Omega)^2]$
F_x	Rotor propulsive force, N
F_z	Rotor lift force, N
M_z	Rotor torque, N.m
M^2C_m	Section pitching moment coefficient
M^2C_n	Section normal force coefficient
Q	Q-criterion, s^{-2}
R	Rotor radius, m
V	Helicopter speed, m/s
v_{iz}	Vertical induced velocity, negative downwash, m/s
v_x, v_y, v_z	Fluid velocity components, m/s
β_{1c}, β_{1s}	Longitudinal and lateral flap angles, °
θ_0, θ_{1c}, θ_{1s}	Collective and cyclic pitch angles, °
μ	Advance ratio, $V/(R\Omega)$
ρ_∞	Freestream air density, kg/m³
σ	Rotor solidity, bRc/A
ψ	Azimuth angle, °
Ω	Rotor angular velocity, rad/s

Acronyms:

BVI	Blade Vortex Interaction
CA	Comprehensive Analysis
CFD	Computational Fluid Dynamics
elsA	*Ensemble Logiciel pour la Simulation en Aérodynamique* (ONERA-SAFRAN CFD code)
HOST	Helicopter Overall simulation Tool (CA code developed by Airbus Helicopters)
MINT	*Marche Instationnaire en Temps* (Time Marching Free Wake model)
STORM	Simulation Tool for Overall Rotorcraft Modeling (CA code, new version of HOST)

2. INTRODUCTION

The demand for rapid and long-range rotorcraft has been growing during the last decades especially in military sector. In order to meet this need, new architectures of rotorcraft dedicated to high-speed have been developed. One of the main solutions to overcome the speed limitation inherent to conventional helicopters consists in combining a main rotor-based

Funded by the European Union. Views and opinions expressed are however those of the authors only and do not necessarily reflect those of the European Union. Neither the European Union nor the granting authority can be held responsible for them.

Funded by the European Union

lift system and a separate propulsion system. The Sikorsky S-97 RAIDER (Ref. 1) and the Airbus Helicopters RACER (Ref. 2) belong to this rotorcraft concept family. The objective of such architectures is to fly at high speed (i.e. above 200 knots) while maintaining maneuverability and payload capability. In consequence, the rotor has to operate efficiently at high thrust, potentially leading to dynamic stall, for a large range of flight conditions. At high-altitude cruise flight, dynamic stall will occur at very high speed and zero or slightly positive rotor shaft angle (i.e. tilted frontward), while, in severe maneuvers, stall usually occurs at moderate speed but for high positive shaft angle (i.e. tilted backward). The dynamic stall limit at moderate speed and close to zero shaft angles is fairly well known since it concerns all the conventional helicopters. However, at very high speed or high positive shaft angle, the stall boundary of the rotor is less clearly defined and further investigations must be conducted in order to guarantee the efficiency and safety of these new rotorcraft concepts.

During the last years, high-fidelity coupling approaches between CFD (Computational Fluid Dynamics) and Comprehensive Analysis (CA) tools have demonstrated very good capabilities for predicting airloads and structural loads on rotor blades under several flight conditions. In the frame of this coupling strategy, the CA code provides the rotor trim and the blade dynamics while the CFD code computes the blade aerodynamic forces. Potsdam et al. (Ref. 3) showed the first satisfactory validations of such coupling simulations, especially for stall conditions. Later, the validation was extended to a slowed rotor at high advance ratios (Ref. 4). Since then, CA/CFD coupling methods have been widely validated on the basis of reference wind-tunnel tests, especially in the frame of a cooperation between US Army and ONERA, for the 7A rotor (Refs. 5 and 6) and more recently for the ERATO rotor (Refs. 7 and 8). A particular attention was paid to the 7A rotor at high thrust and moderate speed in order to identify the mechanisms leading to dynamic stall (Refs. 9, 10 and 11). This work highlighted the crucial role of blade vortex interaction (BVI) as a trigger of stall. This phenomenon was later confirmed for different full–scale rotors under similar conditions, in particular for the UH-60A (Ref. 12) and Bluecopter (Ref. 13).

These studies have contributed to improve the CFD/CA coupling approach that can be considered nowadays as mature and suitable to predict aeroelastic rotor behavior under dynamic stall conditions. On the other hand, low fidelity CA approaches are commonly not considered adapted to predict dynamic stall conditions. However, this conclusion is generally valid with simple induced velocity models that are not capable to capture BVI phenomena while more complex induced velocity models based on a free wake approach could be more adapted. Further investigations are thus needed in order to evaluate the capability of free wake approach to predict high loaded rotors under dynamic stall conditions, especially when BVI is involved.

Therefore, we propose in this paper to investigate the stall boundary of an isolated rotor at low and high advance ratio by means of both low fidelity free wake based CA simulations and high fidelity CA/CFD coupling numerical simulations. The objectives are first to identify the specific features of stall at very high speed in comparison to moderate speed conditions by analyzing the high-fidelity results, and second to evaluate a low fidelity simulation tool by considering the high-fidelity results as reference.

For this analysis, the rotor is set at zero shaft angle with zero longitudinal flap angle. Several simulations with increasing collective pitch angles are performed at both moderate and high advance ratios. A complementary investigation is also proposed in Ref. 15, in which, the advance ratio is kept constant at a moderate value but zero and highly positive shaft angles are considered in order to investigate the effect of a shaft angle increase on the stall features. Both activities are part of the same task of the European Next Generation Rotorcraft Technologies (ENGRT) project funded by the European Union.

3. Numerical setup

3.1. Flight conditions

We consider for this investigation a generic five-bladed rotor. The blades are of constant chord with linear twist, and the tip is of parabolic shape with sweep back. This rotor is fully articulated with lag, flap and pitch hinges.

For the trim law, the advance ratio μ, the rotor shaft angle α_S and the collective pitch angle θ_0 are set as input fixed parameters. Then the cyclic pitch angles θ_{1c} and θ_{1s} are the free parameters that are calculated in order to ensure zero cyclic flap angles ($\beta_{1c} = \beta_{1s} = 0°$).

Two advance ratios are considered: A moderate speed case at $\mu = 0.35$ and a high speed case at $\mu = 0.55$. For each advance ratio, several simulations are performed from low to high collective pitch angles in order to capture the stall onset.

3.2. Low fidelity approach

The low fidelity simulations are performed with the CA tool HOST developed by Airbus Helicopters (Ref. 16). It computes the aero-mechanic behavior of a helicopter for different flight conditions. The last version of this software, called STORM, proposes several improvements, especially a new user interface based on Python modules. However, the kernel of the code remains almost the same. Therefore, we will assume in the rest of this paper that HOST and STORM provide identical results and we will refer to each other indistinctly.

HOST (or STORM) allows to perform several types of simulation: trim calculations to compute the helicopter equilibrium at a prescribed stabilized flight condition, time domain simulations for real-time flight conditions and linear system calculations for helicopter stability studies. For the present activity, only trim calculations will be used. Since this analysis focuses on the main rotor behavior, we will not model all the elements of the rotorcraft in the HOST simulations but only the main rotor considered as an isolated element. The rotor model is composed of an aerodynamic module based on the lifting line theory and a structural dynamics module based on a simplified elastic blade model. To compute the aerodynamic forces, the lifting line theory requires a model to estimate the induced velocity. Several induced velocity models are available in HOST. For this study, we will only consider the free wake model called MINT (*Marche INstationnaire en Temps*) where the wake is modeled as unsteady vortex panels (as described in Refs. 17 and 18). For the MINT simulations, the blade structure is discretized with 25 elements, and the time marching is performed with an azimuthal time step of 6°. The simulations are run during 50 revolutions in order to ensure that the wake and the rotor loads are stabilized. Five revolutions of the wake are preserved in the simulations. MINT simulations with both "rigid" and free wake were first performed. Comparison showed very similar results, because, at such speed conditions, the wake is weakly deformed by its own induced velocity. Therefore, for the rest of this study, only rigid wake STORM/MINT results will be presented, but considered as free wake results.

3.3. High-fidelity approach

The high fidelity aeroelastic simulations are performed with a loose coupling procedure between the CFD solver elsA, property of SAFRAN and ONERA (Ref. 19), and the CA code HOST. The details of this coupling method are described in Ref. 1.

The elsA simulations are based on a Chimera overlapping grids approach. The computational domain is composed of a Cartesian grid in the background (Figure 1.a) and body-fitted grids around the blades (Figure 1.b). The blade grid is composed of 3.2 million elements per blade (208 points along the blade chord, 65 in the wall normal direction and 235 in the spanwise direction). In order to simplify the grid generation, the blade root geometry starts at the first aerodynamic section located while the blade sleeve and the rotor hub are not modeled.

The background grid is composed of 39 million elements and divided in several refinement level blocks. The whole computation domain corresponds to a cube with a dimension of $12R$ (Figure 1.a). In the overlapping region, the Cartesian grid is the finest with a grid cell length of $\Delta x/c = 10\%$ in order to match the blade grid cell at the overlapping edge (Figure 1.c). Previous investigations have shown that this grid resolution provides an adequate preservation of the tip vortices and consequently, a good prediction of the load's fluctuations due to blade vortex interaction (Ref. 20).

The convective flux is discretized with a second order Jameson centered scheme with artificial dissipation. The dissipative coefficients are set to $\chi^{(2)} = 0.5$ and $\chi^{(4)} = 0.008$ as a good compromise between accuracy and robustness. The time integration is performed with a second order implicit Gear scheme. At each time step, the non-linear system is solved iteratively by a Newton method with a maximum number of sub-iterations set to 30. In order to accelerate the convergence of the coupling, the azimuthal time step is set to $\Delta\psi = 1°$ during the first coupling iterations and then reduced to $\Delta\psi = 0.25°$ during the last stages of the coupling in order to improve the accuracy of the simulation. Based on ONERA experience for rotor flow applications, the k-ω turbulence model proposed by Kok (Ref.21) is used together with Menter's SST correction of the eddy viscosity (Ref. 22).

4. COMPARISON BETWEEN LOW AND HIGH-FIDELITY RESULTS

STORM/MINT simulations have been performed at $\mu = 0.35$ and $\mu = 0.55$ at zero shaft angle for a large range of collective pitch angles from -5° to 10°. High fidelity elsA/HOST simulations have been performed for $\theta_0 =$ -1, 1, 4, 5 and 6° at $\mu = 0.35$ and for $\theta_0 =$ 2, 4, 6 and 7° at $\mu = 0.55$. For the elsA/HOST approach, the coupling is performed at each rotor revolution and the simulations is stopped when the control angles and the rotor loads reach close-to-constant values, which occurs after 8 to 10 coupling iterations.

4.1. Rotor loads and control angles

The evolutions of the rotor thrust, drag and torque coefficients with the collective pitch angle are shown in Figure 2. For a more quantitative comparison, the thrust coefficients are also provided in Table 1 and Table 2 for $\mu = 0.35$ and $\mu = 0.55$ respectively. Concerning C_T/σ (Figure 2.a), both high and low fidelity approaches predict the same effect from increasing the advance ratio, i.e. a significant reduction of the thrust levels and of the thrust slope $d(C_T/\sigma)/d\theta_0$. However, a detailed comparison shows noticeable discrepancies. While the agreement between low- and high-fidelity results is satisfactory at the lowest collective, the discrepancy gets more significant when θ_0 increases, as elsA/HOST predicts higher thrust and slope $d(C_T/\sigma)/d\theta_0$ values than STORM/MINT. This observation is similar at both $\mu = 0.35$ and $\mu = 0.55$. Finally, the discrepancy between STORM/MINT and elsA/HOST reaches 9% of the thrust coefficient at the highest collective pitch.

Concerning the power coefficient (Figure 2.b), the conclusions are similar. Both elsA/HOST and STORM/MINT predict a similar strong increase of power when the advance ratio varies from 0.35 to 0.55 (both in terms of slope and values). However, the power increase rate $d(C_P/\sigma)/d(C_T/\sigma)$ is higher with the high-fidelity approach.

Finally, Figure 2.c shows the evolution of the rotor propulsive coefficient. Again, low- and high-fidelity approaches provide similar trends as the advance ratio increases, i.e. a strong increase of the drag force ($C_X/\sigma < 0$) and an increase of the slope $d(C_X/\sigma)/d(C_T/\sigma)$. Consequently, the curves at $\mu = 0.35$ and $\mu = 0.55$ intersect around a thrust coefficient of 0.085 for both numerical approaches. Despite this agreement concerning the general trend of C_X/σ, the two approaches show significant discrepancies in terms of levels. The elsA/HOST simulations predict a lower propulsive force (i.e. higher drag force) than STORM/MINT corresponding to a shift of 0.002 along the C_X/σ axis. As a consequence, the critical thrust coefficient for which $C_X/\sigma = 0$ is significantly different between the two simulations. On one hand, the low fidelity approach predicts that the rotor force gets propulsive for $C_T/\sigma > 0.075$ at $\mu = 0.35$ and for $C_T/\sigma > 0.08$ at $\mu = 0.55$. On the other hand, the high-fidelity approach predicts that the rotor force gets propulsive for $C_T/\sigma > 0.105$ at $\mu = 0.35$ and for $C_T/\sigma > 0.09$ at $\mu = 0.55$.

The cyclic pitch angles are shown in Figure 3. Increasing the advance ratio leads to a significant decrease of the lateral pitch angle θ_{1c}. At $\mu = 0.35$, the agreement between STORM/MINT and elsA/HOST is quite satisfactory. However, at $\mu = 0.55$, a larger discrepancy comprised between $1.5°$ and $2°$ is obtained. Concerning the longitudinal pitch angle, the evolution is less sensitive to the advance ratio and both approaches provide very similar results, with a difference below 1°.

Table 1: Thrust coefficient at $\mu = 0.35$.

θ_0	STORM/MINT	elsA/HOST
-1	0.0672	0.0712
1	0.0840	0.0922
4	0.1026	0.1151
5	0.1062	0.1189
6	0.1089	0.121

Table 2: Thrust coefficient at $\mu = 0.55$.

θ_0	STORM/MINT	elsA/HOST
2	0.0594	0.0618
4	0.0689	0.0749
6	0.0774	0.0862
7	0.0815	0.0902

The azimuthal evolution of the blade thrust is shown for $\mu = 0.35$ and $\mu = 0.55$ in Figure 4 and Figure 5 respectively. At $\mu = 0.35$, STORM/MINT and elsA/HOST results are in very good agreement. The increase of thrust of the rear ($\psi = 0°$) and front ($\psi = 180°$) blades as the collective pitch increases is very similar between the two approaches. However, the CFD results tend to provide slightly higher thrust peak values on the front blade than MINT. On the retreating blade, both approaches show a local minimum (roughly 0.01) that is reached at $\psi = 300°$ corresponding to dynamic stall occurrence. Increasing the collective pitch does not permit to increase this minimum. Therefore, the retreating blade thrust is kept almost constant for all collective pitch angles. On the opposite side of the rotor disk, the advancing blade thrust decreases with the collective pitch. This is due to the negative longitudinal cyclic pitch θ_{1s} that gets more negative in order to maintain the lift of the retreating blade that undergoes dynamic stall.

At $\mu = 0.55$, the agreement between STORM/MINT and elsA/HOST worsens (Figure 5). On the front blade ($\psi = 180°$), high-fidelity results show a thinner and higher thrust peak than low fidelity. In the first quadrant ($0° \leq \psi \leq 90°$), CFD provides high oscillations that do not appear with free wake simulations. At last, STORM/MINT provides a very strong negative blade thrust at $\psi = 90°$, while the thrust remains positive all along the advancing blade side with elsA/HOST.

4.2. Blade section airloads

In order to have a better understanding of the discrepancies between low and high-fidelity approaches, especially at high advance ratio, we propose in this section a more detailed comparison of the numerical results in terms of section normal force coefficient M^2C_n and pitching moment coefficient M^2C_m.

Figure 6 and Figure 7 show rotor maps of M^2C_n at different collective pitch angles obtained at $\mu = 0.35$ by STORM/MINT and elsA/HOST respectively. At this moderate advance ratio, both simulations provide very similar lift distributions along the rotor disk. As the collective pitch increases, two lobes of high M^2C_n on the front ($\psi = 180°$) and rear ($\psi = 0°$) blade tip regions become increasingly intense. The shape of these lobes and the levels of M^2C_n obtained are very similar between STORM/MINT and elsA/HOST. On the advance blade tip, a region of negative lift appears between 90° and 150° of azimuth, which is well captured by both simulations. Figure 8 provides comparisons of the normal force coefficient at six specific blade sections for the highest collective pitch $\theta_0 = 6°$. It confirms that both approaches provide similar trends, but also highlights two main discrepancies. The first one concerns the lift on the blade tip regions of the front and rear blades. At $r/R = 0.97$, elsA/HOST provides higher lift at $\psi = 180°$ and lower lift at $\psi = 0°$ than STORM/MINT does. The second discrepancy concerns the retreating blade that undergoes dynamic stall. Both approaches capture a sudden lift drop that starts at $\psi = 230°$ for $r/R = 0.85$ and at $\psi = 270°$ for $r/R \geq 0.93$. However, the intensity of these lift fluctuations tends to be underestimated by STORM/MINT compared to high fidelity results.

Figure 9 and Figure 10 provide rotor maps of section pitching moment coefficient M^2C_m obtained at $\mu = 0.35$ with STORM/MINT and elsA/HOST respectively. These figures highlight the strong negative pitching moment that appears on the retreating blade and caused by dynamic stall. Two main pitching moment stall events can be distinguished. The first one starts on the inner sections at $\psi = 210°$ and propagates outwards to reach the blade tip at $\psi = 300°$. The second stall event occurs on the blade tip at $\psi = 330°$. It is worth noting that STORM/MINT captures at least qualitatively these two main dynamic stall events. Figure 11 shows the section pitching moments at specific radii that permit a qualitative comparison between the simulations. It confirms that STORM/MINT provides moment stall events in phase with elsA/HOST from inner to outer sections. However, the intensity of the M^2C_m drop is slightly underestimated with low fidelity as previously observed for M^2C_n.

The same analysis is now performed at $\mu = 0.55$. Figure 12 and Figure 13 provide the rotor maps of M^2C_n for all θ_0 obtained with low and high fidelity respectively. As previously observed at lower advance ratio, two main regions of normal force coefficients can be identified, the first one located on the rear blade and the other one on the front blade. However, the exact positions of these high lift regions are shifted compared to the previous case. At moderately speed ($\mu = 0.35$), the lift area of the front blade was located close to the tip and around $\psi = 180°$ (see Figure 6 and Figure 7). Figure 12 and Figure 13 indicate that this area moves inward of the blade ($0.4 \leq r/R \leq 0.6$) and toward the advancing blade ($120° \leq \psi \leq 150°$) when the advance ratio increases. This behavior is very similar to what Potsdam *et al.* observed for the slowed UH-60A rotor in Ref. 4. It is worth mentioning that both STORM/MINT and elsA/HOST provide this trend. Consequently, this lift region is now located close to the azimuthal portion that undergoes negative lift at blade tip. For elsA/HOST simulations (Figure 13), both the outward negative lift region and the inward positive lift region occur at the same azimuthal position. These two regions balance each other, explaining why the net thrust of the advancing blade remains positive in Figure 5.b. On the other hand, STORM/MINT (Figure 12) provides an outward negative lift region for $90° \leq \psi \leq 120°$ and an inward positive lift region for $120° \leq \psi \leq 150°$. Located in distinct azimuthal regions, the two effects do not balance each other. Therefore, the net thrust provided by STORM/MINT on the advancing blade gets first strongly negative and then positive (Figure 5.a). On the rear blade region, it is interesting to note that the lift is “crosshatched” thus undergoing two or three oscillations. This phenomenon is observed with both STORM/MINT (Figure 12) and elsA/HOST (Figure 13), although the intensity is stronger in the high fidelity results. Figure 14 shows a quantitative comparison of M^2C_n at several blade sections for the highest collective pitch case. The inward positive lift region is clearly visible at the sections $r/R = 0.44$ and $r/R = 0.58$ for $120° \leq \psi \leq 150°$, while the outward negative lift region can be seen at $r/R \geq 0.85$ for $90° \leq \psi \leq 120°$. STORM/MINT and elsA/HOST provide very similar results in these two regions.

The rotor maps of section pitching moment coefficients obtained at $\mu = 0.55$ with STORM/MINT and elsA/HOST are shown in Figure 15 and Figure 16 respectively. Similarly to what was observed at $\mu = 0.35$, the retreating blade undergoes a strong negative pitching moment due to dynamic stall. Both low and high-fidelity approaches predict this phenomenon but the intensity of the M^2C_m drop is underestimated with STORM/MINT. As shown in Figure 17, the tip sections ($r/R = 0.93$ and $r/R = 0.97$) reach a pitching moment coefficient of -0.03 with elsA/HOST against -0.02 for the free wake approach. In the reverse flow region, the high-fidelity results (Figure 16) highlight a strong positive pitching moment that was not observed at lower advance ratio. This phenomenon is also visible with the STORM/MINT results (Figure 15) but with significantly lower levels. Figure 17 shows that elsA/HOST predicts a maximum M^2C_m of 3×10^{-3} at $r/R = 0.44$ against 5×10^{-4} with STORM/MINT. This strong positive pitching moment in the reverse flow region is a specific characteristic of high advance ratio. It was first observed by Potsdam et al. for the slowed UH-60A rotor (Ref. 4) in both experiments and high-fidelity simulations. Later, Öhrle et al. showed the same behavior with a high fidelity simulation of the RACER at high speed forward flight (Ref. 23). The authors showed that this noise-up pitching moment is due to a vortex shedding from the trailing edge in the lower side of the blade. The pitching moment also shows unusual behavior on the advancing blade. A region of strong positive M^2C_m is observed on the blade tip ($r/R > 0.8$) for $90° \leq \psi \leq 120°$ where the lift is strongly negative. More inward ($0.6 \leq r/R \leq 0.8$), where the lift is positive, the pitching moment gets negative. This characteristic is observed on both high and low fidelity results, but STORM/MINT tends to overestimate the positive pitching moment peak at the blade tip. Furthermore, STORM/MINT also predicts a strong negative M^2C_m on the blade tip region for $40° \leq \psi \leq 80°$, that does not appear in elsA/HOST results. Figure 17 shows that this negative peak reaches -0.045 at $r/R = 0.97$. This unexpected negative pitching moment observed with STORM/MINT for $40° \leq \psi \leq 80°$ at $\mu = 0.55$ does not appear at $\mu = 0.35$. In order to understand the origin of this problem, the induced velocity fields obtained at both advance ratios are compared in Figure 18. It reveals that a tiny region of high upwash induced velocity appears at $\mu = 0.55$ at the advancing blade tip and reaches 20 m/s at $\psi = 85°$. This high level of induced velocity leads to a local increase of the angle of attack associated with a strong negative pitching moment. This phenomenon is localized to a narrow azimuthal region. For $\psi \geq 90°$, the induced velocity reaches lower values and the M^2C_m follows a trend similar to the high-fidelity results. Thus, the erroneous spot of high positive pitching moment observed for $40° \leq \psi \leq 80°$ is clearly due to this localized spot of upwash flow. Further investigation should be conducted to understand the dynamics of the free wake model in this region. Despite this unexpected behavior of STORM/MINT on the advancing blade tip, Figure 17 shows that the low-fidelity approach predicts the trends of elsA/HOST with a good agreement.

5. ANALYSIS OF THE HIGH-SPEED FLOW FEATURES

The comparison of the airloads has revealed some usual characteristics that appear at $\mu = 0.55$, which are outlined below:

- The advancing blade undergoes a strong negative lift and noise-up pitching moment at the blade tip together with a strong positive lift and a noise-down pitching moment at mid span.
- The retreating blade outer sections experience a strong noise-down pitching moment

due to dynamic stall that looks similar to the moderate advance ratio case.
- The retreating blade inner sections experience a strong noise-up pitching moment in the reverse flow region.
- The rear blade is subject to lift oscillations all along the span for $0° \leq \psi \leq 30°$.

We propose in this section to analyze the high-fidelity results in more detail in order to better understand the origins of the phenomena listed above.

5.1. Advancing blade

To understand the unusual airloads of the advancing blade at very high advance ratio, it is necessary to pay attention to the rotor wake. Figure 19 provides views of the tip vortex of the blade located at $\psi = 162°$. At both advance ratios, this tip vortex impinges perpendicularly the following blade located at $\psi = 90°$. Since the lift of the blade tip in the third quadrant is negative, the emitted vortex is rotating “the wrong way down”, as indicated by the circular arrows in Figure 19. Consequently, this vortex induces positive fluid velocity (i.e. upwash) inboard of the blade located at $\psi = 90°$ and negative fluid velocity (i.e. downwash) outboard. Figure 19 shows that the intensity of the induced vertical velocity is much stronger at $\mu = 0.55$ than $\mu = 0.35$. Furthermore, the trajectory of the vortex is slightly different between the two advance ratios. At $\mu = 0.55$, the vortex moves inboard which increases the intensity of the interaction. Therefore, at high advance ratio, the inboard sections of the advancing blade undergo a strong upwash effect that increases the local angle of attack, leading to positive lift and negative pitching moment. On the other hand, the outboard sections undergo a strong downwash effect leading to negative lift and positive pitching moment. Thus, the distributions of M^2C_n and M^2C_m on the advancing blade (Figure 13 and Figure 16) seem clearly correlated to the effect of this perpendicular BVI phenomenon.

5.2. Dynamic stall of the retreating blade tip

Figure 20 provides rotor maps of the chordwise position of flow separation at $\mu = 0.35$ for different collective pitch angles. For $\theta_0 \leq 1°$, flow separation first appears on the middle blade sections ($0.4 \leq r/R \leq 0.8$) between $180°$ and $270°$ of azimuth. Separation point starts at mid chord and moves progressively toward the leading edge. For $\theta_0 \geq 4°$, this flow separation region spreads toward the blade tip in the azimuthal portion $240° \leq \psi \leq 360°$. In the tip region, the flow separation is more abrupt and starts at the leading edge. A second dynamic stall event also appears for $0 \leq \psi \leq 45°$ on the blade tip region. All these flow separation regions perfectly correlate with the negative M^2C_m regions observed in Figure 10 and Figure 11. This shows that all the strong noise-down pitching moment events at $\mu = 0.35$ are clearly correlated to flow separations.

Figure 21 shows the chordwise position of flow separation at $\mu = 0.55$. These rotor maps provide characteristics similar to those observed at lower advance ratio. Flow separation starts inboard of the retreating blade and spreads toward the blade tip as the collective pitch increases. However, increasing the advance ratio leads to an earlier flow separation at blade tip that occurs at $\psi = 210°$ at $\mu = 0.55$ instead of $\psi = 240°$ at $\mu = 0.35$. Furthermore, the massive flow separation region is larger at high advance ratio although the rotor thrust coefficient reaches lower values.

In order to identify the role of BVI in dynamic stall triggering, Figure 22 and Figure 23 provide a view of rotor wake vortices together with the vertical fluid velocity on a slice located just below the rotor plane. These figures allow to quantify the intensity of the downwash and upwash velocities induced on both sides of the wake vortices.

Figure 22 shows the same snapshot obtained at low and high collective pitch angles for $\mu = 0.35$. The retreating blade located at $\psi = 306°$ is undergoing a parallel interaction with the tip vortex emitted by the preceding blade. At low collective pitch (Figure 22.a), this interaction has a weak effect on the airloads. However, at high collective (Figure 22.b), the upwash effect of the tip vortex leads to an abrupt increase of the local angle of attack leading to stall. Thus, stall vortices are shed and can be easily distinguished from the tip vortex in Figure 22.b, as they are smaller, more tridimensional and with higher vorticity levels. The same scenario of BVI-induced dynamic stall reported in Refs. 9, 10, 11 and 12.

Figure 23 shows similar flow field views at $\mu = 0.55$, for both low and high collective pitch angles. Due to the higher advance ratio, the tip vortex follows a different trajectory in the retreating blade side and moves faster downstream. Consequently, the retreating blade never goes through the tip vortex emitted by the preceding blade as it was observed at lower μ. At high collective pitch (Figure 23.b), flow separates on the retreating blade located at $\psi = 306°$, while several intense and tridimensional stall vortices are shed. Stall thus occurs without *a priori* any BVI phenomenon. However, the velocity field shown in Figure 23.b reveals that the preceding tip vortex induces a positive velocity between 6 to 8 m/s just above of the retreating blade. This upwash effect does not seem significant but since the relative velocity of the retreating blade is reduced when the advance ratio increases, this vertical induced velocity could contribute to an increase of the local angle of attack between 5 and $10°$. In combination with both collective and cyclic pitch increase, the induced effect of the tip vortex could be sufficient to trigger dynamic stall, although the blade never directly impinges the vortex.

5.3. Reverse flow region

Figure 24 shows the vorticity magnitude at several radial slices along the retreating blade ($\psi = 306°$) at high μ and high θ_0. At $r/R = 0.92$, the flow is massively separated and the strong vorticity of the stall vortex is clearly visible. At $r/R = 0.72$, the flow has already reattached as indicated by the thin region of vorticity in the close vicinity of the blade wall. The section located at $r/R = 0.55$ is at the limit of the reverse flow region where the relative velocity is close to zero. A strong trailing edge (TE) vortex appears on the lower side of the blade. Furthermore, at the edge of the reverse flow, the blade section lift moves from positive to negative. Consequently, a large but weak vortex is emitted in the wake and convected downstream the leading edge of the radial section $r/R = 0.55$. It is referred-to as reverse flow vortex in Figure 24. The most inboard sections ($r/R = 0.35$) is located inside the reverse flow region. The TE vortex is shed downsteam in the wake, which is responsible of the strong positive pitching moment observed in Figure 16 and Figure 17.

5.4. Rear blade

Figure 23.a highlights three rows of blade root vortices. Because of the high advance ratio, these vortices' trajectories are quasi-aligned with the x-axis. Those flow structures are still easily visible at high collective pitch in Figure 23.b although they are not indicated. For both collective pitch angles, these vortices induce strong positive and negative velocities on each of their sides. Another view of these root vortices is proposed in Figure 25. The induced velocity is here shown on a slice perpendicular to the vortices' axis in order to highlight the induced vertical velocity. The rows of these root vortices clearly lead to a series of highly positive and negative vertical velocities. This vertical velocity field will clearly leads to oscillations of the angle of attack of the blade passing through this region, which explains the lift fluctuations observed on the inboard sections of the rear blade in Figure 16 and Figure 17.

6. CONCLUSIONS

Low and high fidelity simulations have been conducted for a generic isolated rotor at both moderate ($\mu = 0.35$) and high ($\mu = 0.55$) advance ratios. Low fidelity approach is based on the free wake model called MINT within STORM Comprehensive Analysis code. The high-fidelity approach is based on a loose coupling between elsA CFD solver and HOST Comprehensive Analysis tool. For each advance ratio, a large sweep of the collective pitch is performed in order to simulate rotor stall onset. This numerical investigation has permitted first to evaluate the prediction capability of the low fidelity approach with respect to high fidelity results and second, to describe in details the flow characteristics specific to high advance ratio. The comparison between low and high fidelity results leads to the following conclusions:

- The STORM/MINT free wake approach predicts the good trend in terms of rotor thrust, drag and power coefficients with increasing collective pitch, at both advance ratios. However, the increases of thrust and power are slightly underestimated compared to CFD results, while the drag force is more significantly underestimated.
- At moderate collective pitch angle, STORM/MINT and elsA/HOST predict similarly the variations of the thrust distribution on the rotor disk as the advance ratio increases, especially on the advancing blade that is subject to a strong lift increase on the inboard sections and a strong negative lift on the outboard sections.
- At high advance ratios, the rear blade undergoes lift oscillations with both approaches that are not observed at moderate speed.
- At high advance ratio, STORM/MINT predicts a strong pitching moment negative peak at $\psi = 80°$ that does not appear with CFD and seems to be due to an excessive positive induced velocity spot. However, for $90° \leq \psi \leq 180°$, the CFD

evolution of the pitching moment is well reproduced by the free wake approach.

- The comparison of the airloads indicates that STORM/MINT predicts qualitatively, for both advance ratios, the occurrence of lift and pitching moment drop on the retreating blade due to dynamic stall as the collective pitch increases. However, the intensity of stall is underestimated by low fidelity approach.

The analysis of the flow characteristics at high advance ratio leads to the following conclusions:

- The advancing blade undergoes a strong negative lift and noise-up pitching moment at the blade tip together with a strong positive lift and a noise-down pitching moment at mid span. This loads distribution is due to a perpendicular interaction of the blade with the preceding blade tip vortex that rotates in the opposite direction because of the negative lift distribution on the advance blade tip.
- The retreating blade outboard sections experience a strong noise-down pitching moment due to dynamic stall for both advance ratios. At $\mu = 0.35$, this stall is clearly triggered by a parallel interaction with the preceding blade tip vortex. At high advance ratio, no BVI is observed during dynamic stall, but the CFD results indicate that the tip vortex, although far from the blade, induces non-negligible upwash velocities on the blade that could contribute to stall onset.
- The retreating blade inner sections experiences a strong noise-up pitching moment in the reverse flow region that is due to the shedding of a trailing edge vortex on the lower side.
- The rear blade is subject to lift oscillations all along the span for $0° \leq \psi \leq 30°$ that is due to BVI with several rows of root vortices emitted by the three preceding blades.

This investigation was mainly focused on the aerodynamic results. In the continuity of this project, it is planned to analyze in details the results in terms of structural loads. Furthermore, the simulations will be pursued for intermediate advance ratio ($\mu = 0.45$) and including propulsive (i.e. tilted forward) rotor conditions.

Author contact:

François Richez: francois.richez@onera.fr

Joëlle Bailly: joelle.bailly-zibi@onera.fr

Ilyès Berhouni: ilyes.berhouni@onera.fr

7. ACKNOWLEDGMENTS

The authors would like to acknowledge the European Union that has funded this research activity in the frame of the ENGRT (European Next Generation Rotorcraft Technology) project and Manousos Kelaidis from Airbus Helicopters for his sound advice during this study.

8. REFERENCES

1. Lorber, P., F., Law, G., K., O'Neill, J., J., Matalanis, C., Bowles, P., "Overview of S-97 RAIDER™ Scale Model Tests", 72nd American Helicopter Society Annual Forum, West Palm Beach, Florida, USA, May 2016.

2. Eglin, P., Emacher, M., Desvigne, D., Roca Leon, E., "Airbus RACER High speed Demonstrator Flight Tests", 81st Vertical Flight Society Annual Forum, Virginia Beach, Virginia, USA, May, 2025.

3. Potsdam, M., Yeo, H., and Johnson, W., "Rotor Airloads Prediction Using Loose Aerodynamic/Structural Coupling", *Journal of Aircraft*, Vol. 43, (3), May-June 2006, DOI: 10.2514/1.14006

4. Potsdam, M., Datta, A. and Jayaraman, B., "Computational Investigation and Fundamental Understanding of a Slowed UH-60A Rotor at High Advance Ratios," *Journal of the American Helicopter Society,* Vol. 61, No. 2, April 2016, pp. 1-17(17), DOI : 10.4050/JAHS.61.022002

5. Ortun, B., Potsdam, M., Yeo, H., Van Truong, K., "Rotor Loads Prediction on the ONERA 7A Rotor Using Loose Fluid/Structure Coupling", *Journal of the American Helicopter Society*, Vol. 62(3), pp. 1-13, 2017, DOI: 10.4050/F-0072-2016-11370

6. Yeo, H., Potsdam, M., Ortun, B. and Van Truong, K., "High-Fidelity Structural Loads Analysis of the ONERA 7A Rotor," *Journal of Aircraft*, Vol. 54, No. 5, 2017, DOI: 10.2514/1.C034286

7. Balmaseda, M., Yeo, H., Richez, F. Jayaraman, B., Ortun, B., "High-fidelity aerodynamic loads analysis of the double-swept ERATO rotor", 50th European Rotorcraft Forum, Marseille, France, September 10-12, 2024.

8. Yeo, H., Balmaseda, M., Jayaraman, B., Richez, F., Ortun, B., "High-Fidelity structural loads analysis of the double-swept ERATO ro-

tor", 50th European Rotorcraft Forum, Marseille, France, September 10-12, 2024.

9. Richez, F., “Analysis of Dynamic Stall Mechanisms in Helicopter Rotor Environment”, *Journal of the American Helicopter Society*, Vol. 63, No. 2, April 2018, pp. 1-11, DOI: 10.4050/JAHS.63.022006

10. Castells, C., Richez, F. and Costes, M., “A Numerical Analysis of the Dynamic Stall Mechanisms on a Helicopter Rotor from Light to Deep Stall”, *Journal of the American Helicopter Society*, Vol. 65, No. 3, July 2020, pp. 1-17, DOI: 10.4050/JAHS.65.032005

11. Castells, C., Richez, F. and Costes, M., “A Numerical Investigation of the Influence of the Blade–Vortex Interaction on the Dynamic Stall Onset”, *Journal of the American Helicopter Society*, Vol. 66, 032001, Mai 2021, DOI: 10.4050/JAHS.66.032001

12. Richez, F., Jain, R., Smith, M., Grubb, A., Castells, C., “Validation and Analysis of Aeroelastic Simulations of the UH-60A Rotor from Pre- to Post-stall Flight Conditions”, Vertical Flight Society’s 76th Annual Forum & Technology Display, Virginia Beach, VA, US, October 6-8, 2020.

13. Letzgus, J., Keßler, M. and Krämer, E., “Simulation of Dynamic Stall on an Elastic Rotor in High-Speed Turn Flight,” *Journal of the American Helicopter Society*, Vol. 65, No. 2, April 2020, pp. 1-12(12), DOI: 10.4050/JAHS.65.022002

14. Madeira, A., Roucoules, L., Malburet, F., Serr C., Kelaidis, M., "Numerical analysis of helicopter’s blade pitch link loads", 46th European Rotorcraft Forum, Moscow, Russia, September 8-11, 2020.

15. Berhouni, I., Bailly, J., Richez, F., "Evaluation of Shaft Angle Effects on Dynamic Stall Based on Low and High Fidelity Aero-Elastic Rotor Simulations", 51st European Rotorcraft Forum, Venice, Italy, September 9-12, 2025.

16. Benoit, B., Dequin, A.-M., Kampa, K., Von Grünhagen, W., Basset, P.-M., and Gimonet, B., “HOST, a General Helicopter Simulation Tool for Germany and France”, 56th American Helicopter Society Annual Forum, Virginia Beach, Virginia, USA, May 2000.

17. Mudry, M., “*La théorie générale des nappes et filaments tourbillonnaires et ses applications à l’aérodynamique instationnaire*”, PhD thesis, Université de Paris VI, Juillet 1982.

18. Le Bouar-Coppens, G., Costes, M., Leroy-Chesneau, A. and Devinant, P., “Numerical simulations of unsteady aerodynamics of helicopter rotor in maneuvering flight conditions”, *Aerospace Science and Technology*, Vol. 8, pp.11-25, 2004.

19. Cambier, L., Heib, S., Plot, S., “The ONERA elsA CFD software: input from research and feedback from industry”, *Mechanics & Industry*, Vol. 14 (3), 2013, pp. 159-174, DOI: 10.1051/meca/2013056

20. Chaderjian, N., M., “Navier-Stokes Simulation of UH-60A Rotor/Wake Interaction Using Adaptive Mesh Refinement”, 73rd American Helicopter Society, Fort Worth, TX, USA, May 9-11, 2017.

21. Kok J.-C., “Resolving the Dependence on Freestream Values for the k-ω Turbulence Model,” in *AIAA Journal*, Vol. 38, 2000, pp. 1292–1295, DOI: 10.2514/2.1101

22. Menter, F. R., “Two-Equation Eddy-Viscosity Transport Turbulence Model for Engineering Applications,” *AIAA Journal*, Vol. 32, Issue 8, pp. 1598–1605, 1994, DOI: 10.2514/3.12149

23. Öhrle, C., Frey, F., Thiemeier, J., Keßler, M., and Krämer, E., “Coupled and Trimmed Aerodynamic and Aeroacoustic Simulations for Airbus Helicopters’ Compound Helicopter RACER,” *Journal of the American Helicopter Society*, Vol. 64, (3), July 2019, pp. 1–14. DOI: 10.4050/jahs.64.032003

9. CLASSIFICATION & COPYRIGHT

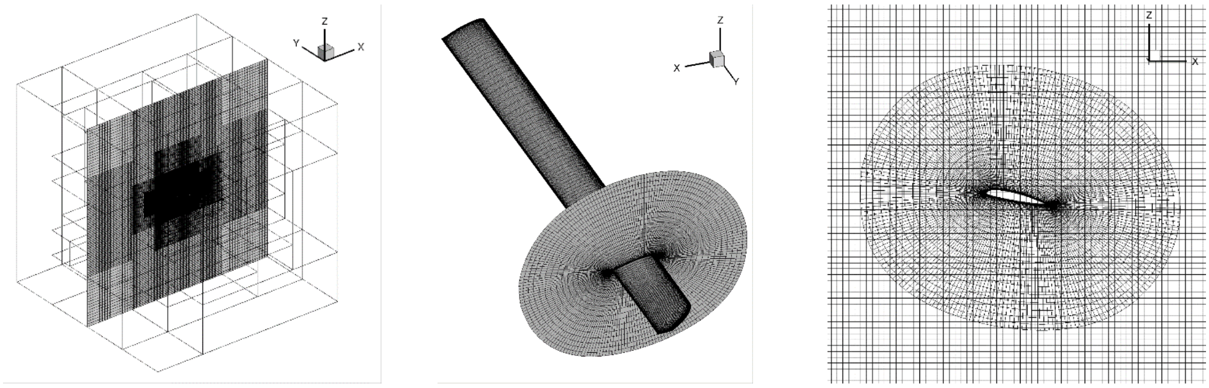

a) Cartesian background grid *b)* Blade body-fitted grid *c)* Overlapping grid region

Figure 1: Overview of the CFD grids.

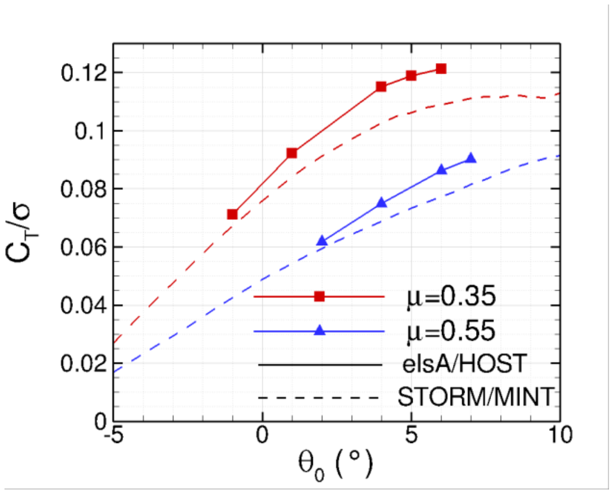

a) Thrust coefficient.

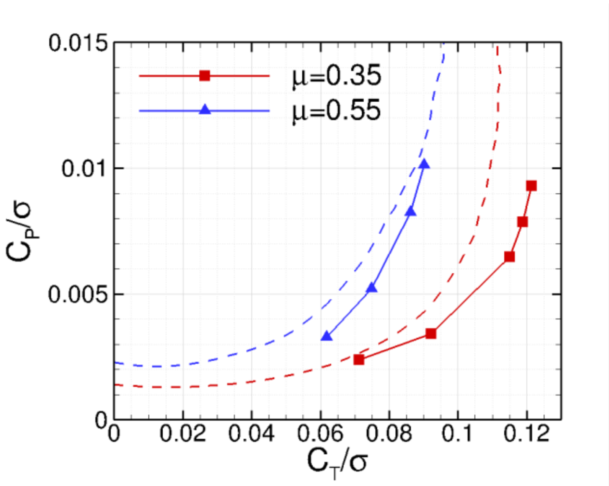

b) Power coefficient.

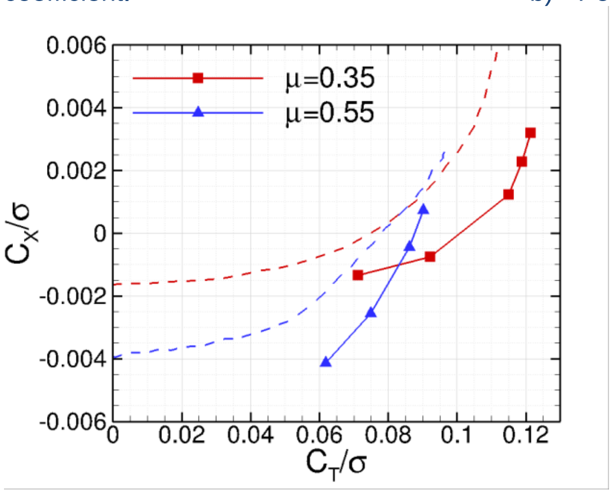

c) Propulsive coefficient.

Figure 2: Evolution of rotor lift, power and propulsive coefficients with collective pitch angle at $\mu = 0.35$ and 0.55 (elsA/HOST: solid lines, STORM/MINT: dash lines).

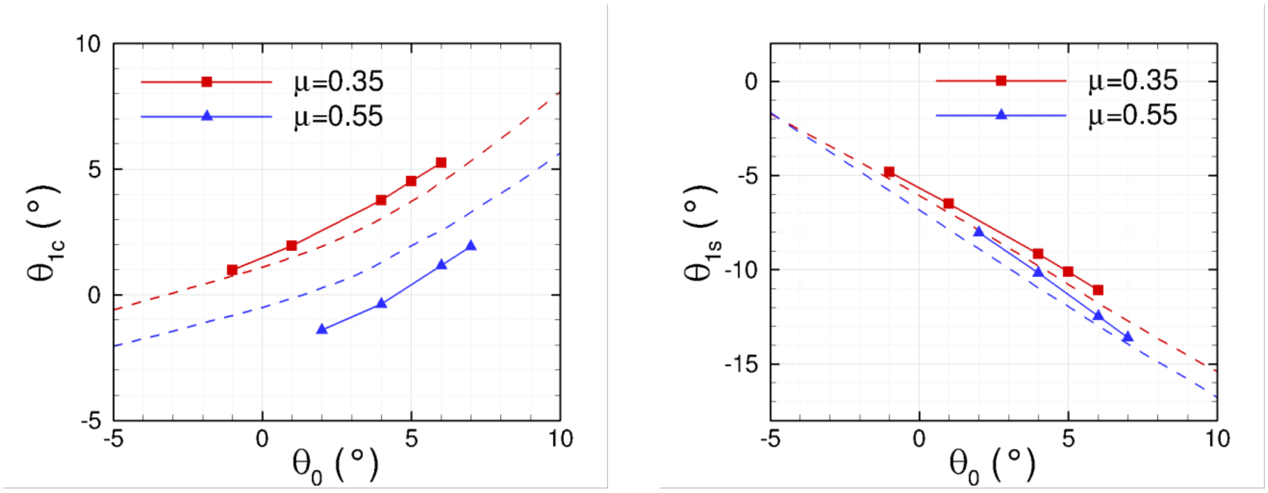

a) Lateral pitch angle.
b) Longitudinal pitch angle.

Figure 3: Evolution of the cyclic pitch angles with collective pitch at $\mu = 0.35$ and 0.55 (elsA/HOST: solid lines, STORM/MINT: dash lines).

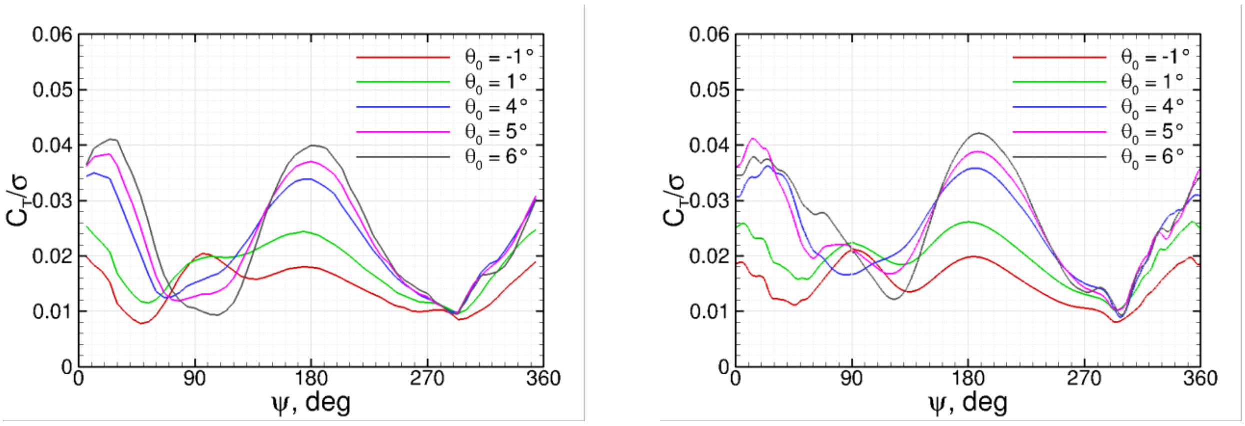

a) STORM/MINT.
b) elsA/HOST coupling.

Figure 4: Blade thrust coefficient as a function of azimuth at moderate advance ratio $\mu = 0.35$.

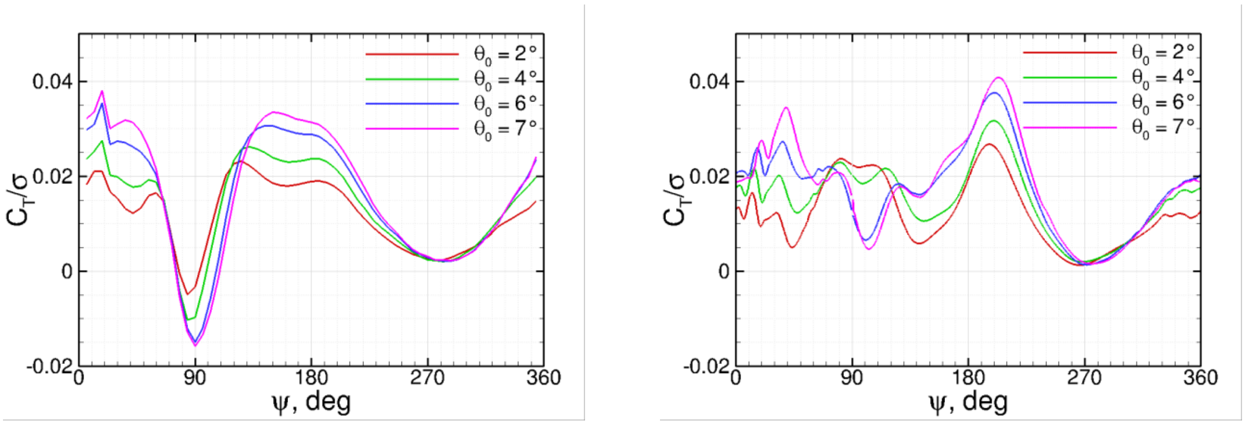

a) STORM/MINT.
b) elsA/HOST coupling.

Figure 5: Blade load coefficient as a function of azimuth at very high advance ratio $\mu = 0.55$.

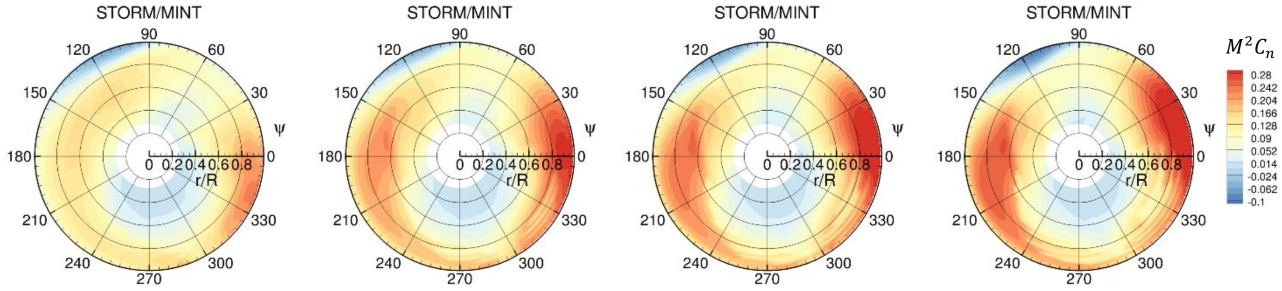

a) $\theta_0 = 1°$, $C_T/\sigma = 0.0840$

b) $\theta_0 = 4°$, $C_T/\sigma = 0.1026$

c) $\theta_0 = 5°$, d) $C_T/\sigma = 0.1062$

e) $\theta_0 = 6°$, $C_T/\sigma = 0.1089$

Figure 6: Low fidelity prediction of section normal coefficient at $\mu = 0.35$ (STORMMINT).

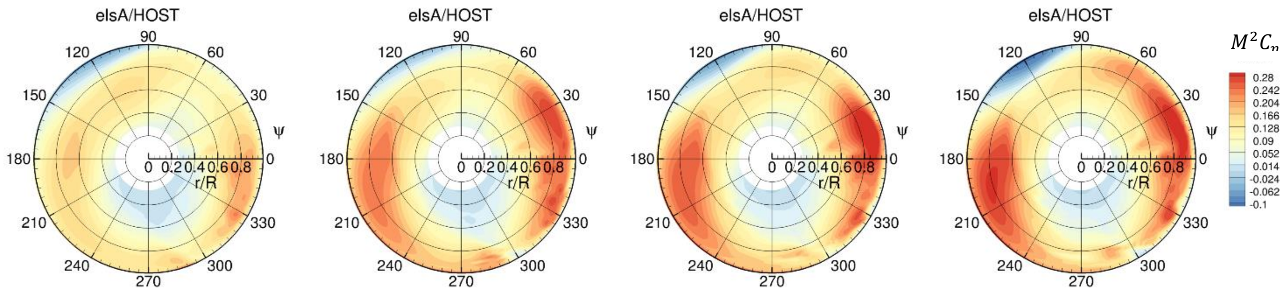

a) $\theta_0 = 1°$, $C_T/\sigma = 0.0922$

a) $\theta_0 = 4°$, $C_T/\sigma = 0.1151$

b) $\theta_0 = 5°$, $C_T/\sigma = 0.1189$

c) $\theta_0 = 6°$, $C_T/\sigma = 0.121$

Figure 7: High-fidelity prediction of section normal force coefficient at $\mu = 0.35$ (elsA/HOST coupling).

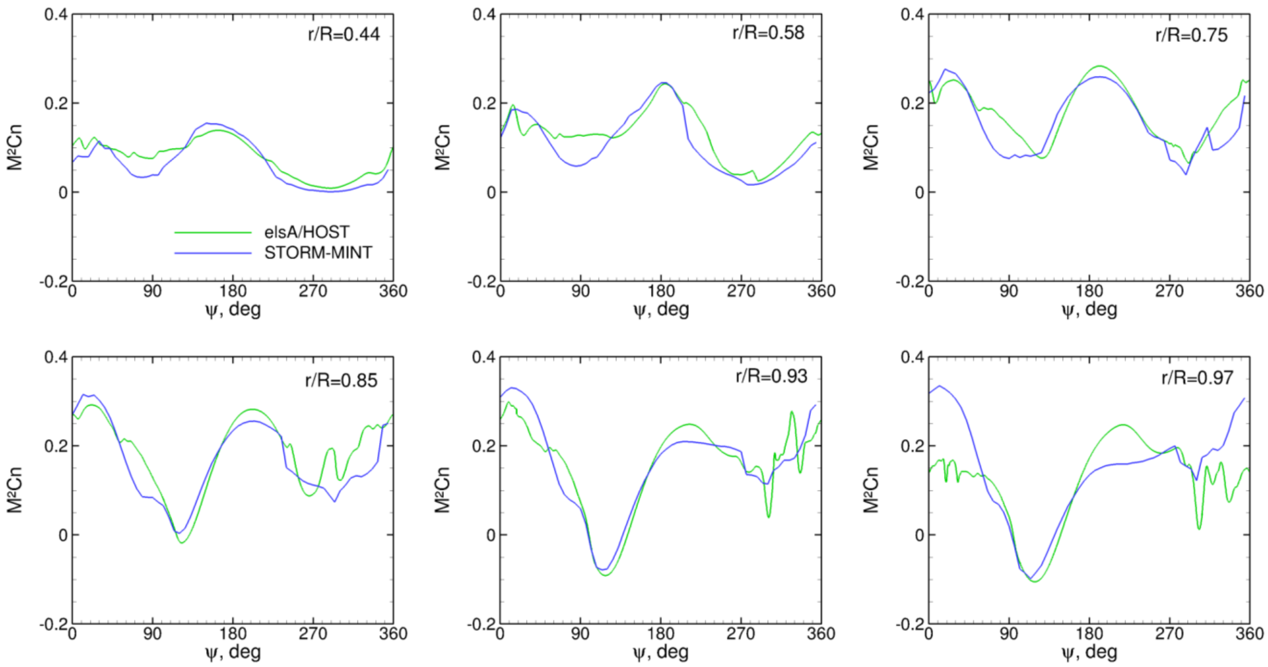

Figure 8: Section normal force coefficient at $\mu = 0.35$ and $\theta_0 = 6°$ (MINT: $C_T/\sigma = 0.1089$, elsA: $C_T/\sigma = 0.121$).

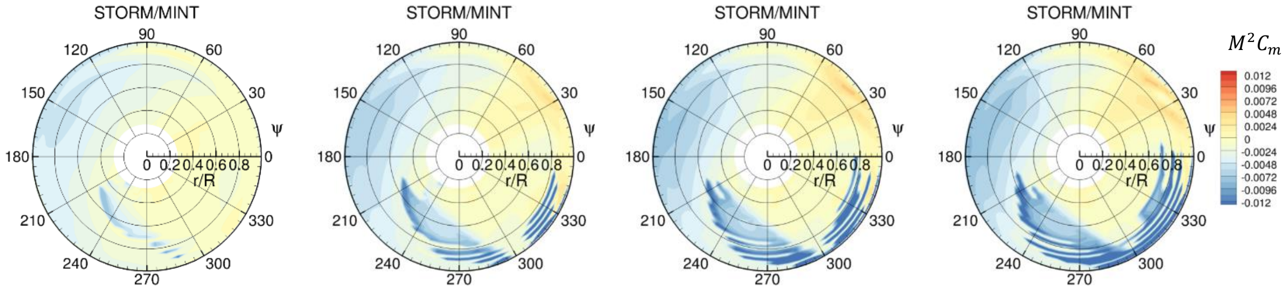

a) $\theta_0 = 1°$, $C_T/\sigma = 0.0840$ *b)* $\theta_0 = 4°$, $C_T/\sigma = 0.1026$ *c)* $\theta_0 = 5°$, $C_T/\sigma = 0.1062$ *d)* $\theta_0 = 6°$, $C_T/\sigma = 0.1089$

Figure 9: Low fidelity prediction of section pitching moment coefficient at $\mu = 0.35$ (STORM/MINT).

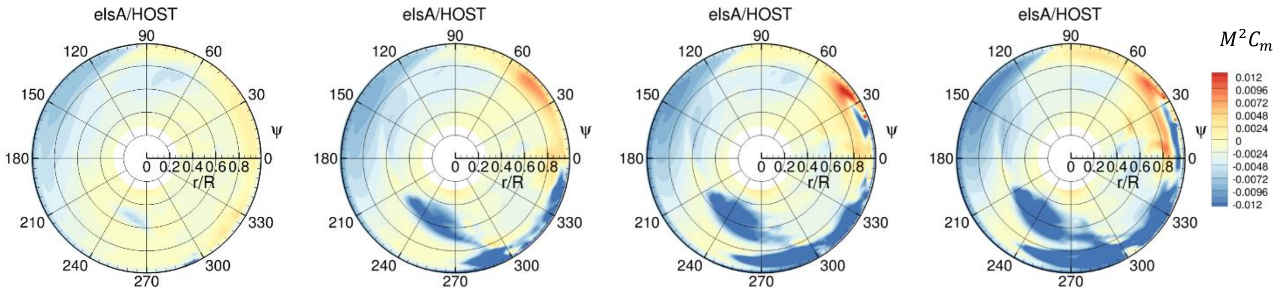

a) $\theta_0 = 1°$, $C_T/\sigma = 0.0922$ *b)* $\theta_0 = 4°$, $C_T/\sigma = 0.1151$ *c)* $\theta_0 = 5°$, $C_T/\sigma = 0.1189$ *d)* $\theta_0 = 6°$, $C_T/\sigma = 0.121$

Figure 10: High-fidelity prediction of section pitching moment coefficient at $\mu = 0.35$ (elsA/HOST coupling).

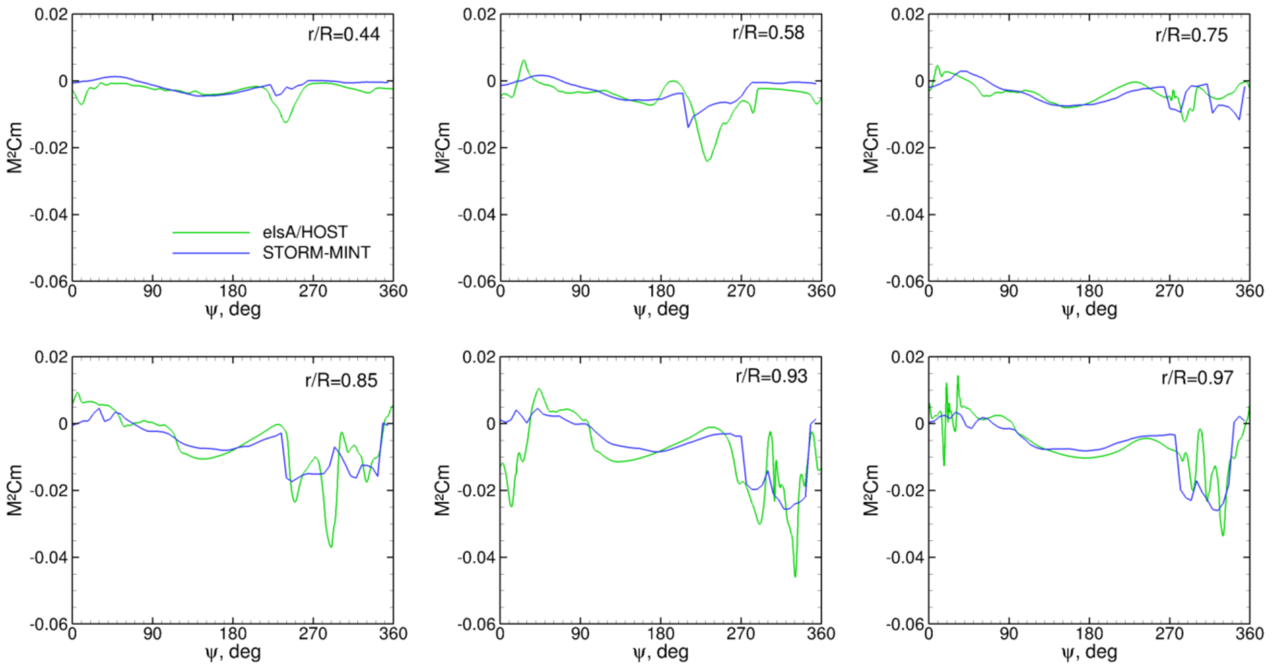

Figure 11: Section pitching moment coefficient at $\mu = 0.35$ and $\theta_0 = 6°$ (MINT: $C_T/\sigma = 0.1089$, elsA: $C_T/\sigma = 0.121$).

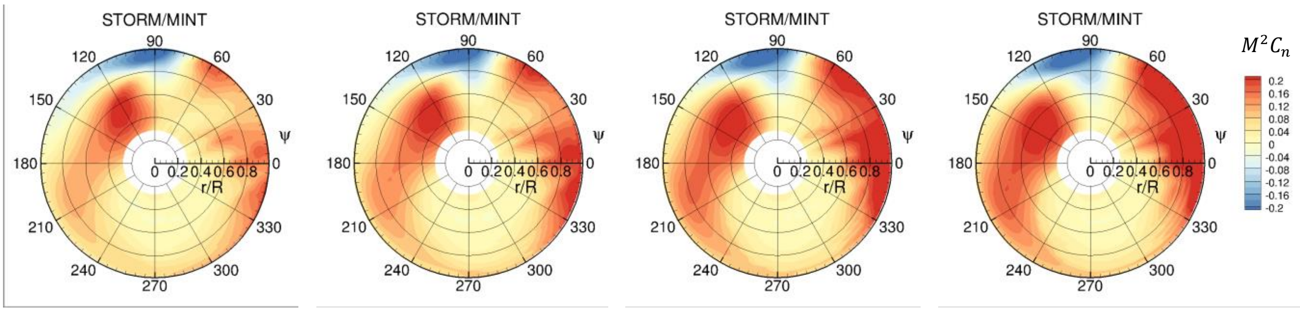

a) $\theta_0 = 2°$, $C_T/\sigma = 0.0594$
b) $\theta_0 = 4°$, $C_T/\sigma = 0.0689$
c) $\theta_0 = 6°$, $C_T/\sigma = 0.0774$
d) $\theta_0 = 7°$, $C_T/\sigma = 0.0815$

Figure 12: Low fidelity prediction of section normal coefficient at $\mu = 0.55$ (STORM-Freewake).

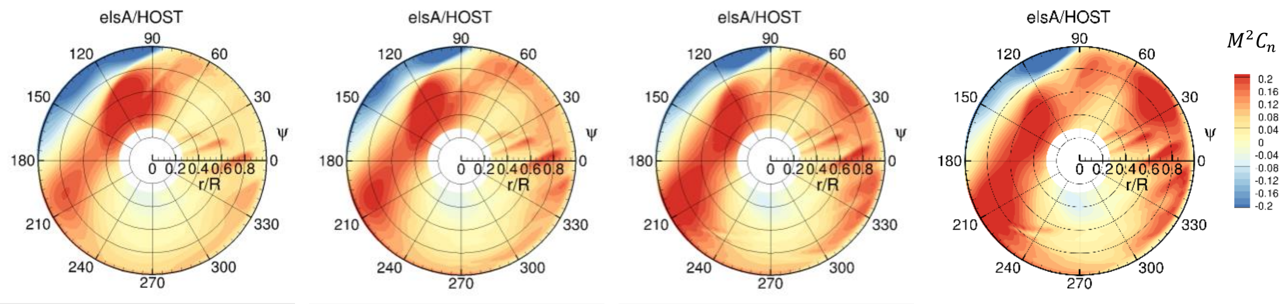

a) $\theta_0 = 2°$, $C_T/\sigma = 0.0618$
b) $\theta_0 = 4°$, $C_T/\sigma = 0.0749$
c) $\theta_0 = 6°$, $C_T/\sigma = 0.0862$
d) $\theta_0 = 7°$, $C_T/\sigma = 0.0902$

Figure 13: High-fidelity prediction of section normal force coefficient at $\mu = 0.55$ (elsA/HOST coupling).

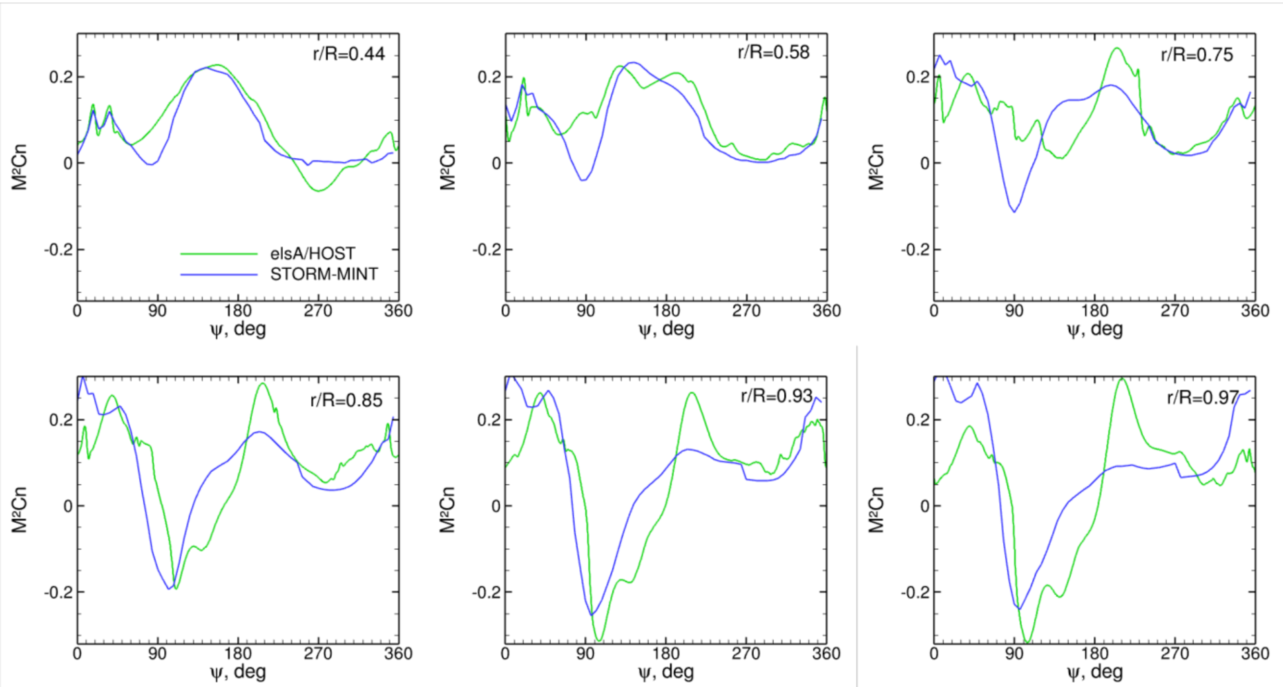

Figure 14: Section normal force coefficient at $\mu = 0.55$ and $\theta_0 = 7°$ (MINT: $C_T/\sigma = 0.0815$, elsA: $C_T/\sigma = 0.0902$).

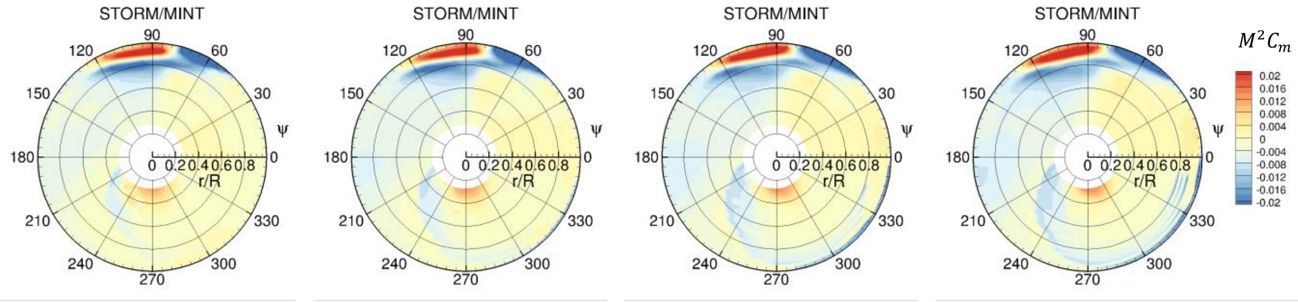

a) $\theta_0 = 2°$, $C_T/\sigma = 0.0594$

b) $\theta_0 = 4°$, $C_T/\sigma = 0.0689$

c) $\theta_0 = 6°$, $C_T/\sigma = 0.0774$

d) $\theta_0 = 7°$, $C_T/\sigma = 0.0815$

Figure 15: Low fidelity prediction of section pitching moment coefficient at $\mu = 0.55$ (STORM/MINT).

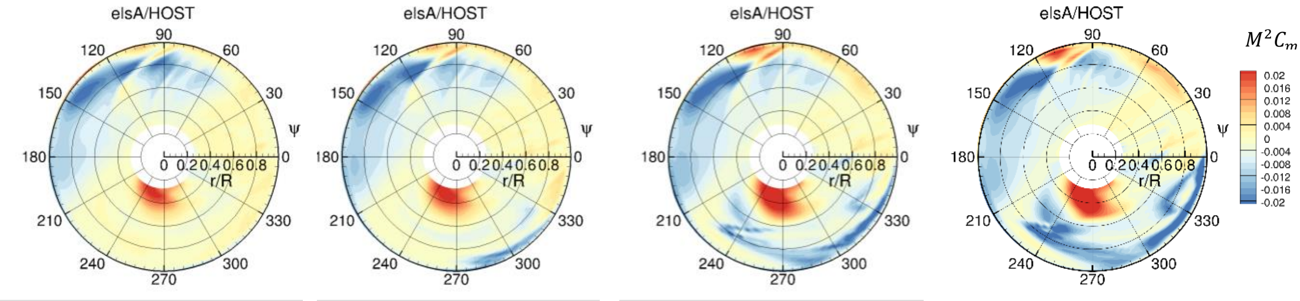

a) $\theta_0 = 2°$, $C_T/\sigma = 0.0618$

b) $\theta_0 = 4°$, $C_T/\sigma = 0.0749$

c) $\theta_0 = 6°$, $C_T/\sigma = 0.0862$

d) $\theta_0 = 7°$, $C_T/\sigma = 0.0902$

Figure 16: High-fidelity prediction of section pitching moment coefficient at $\mu = 0.55$ (elsA/HOST coupling).

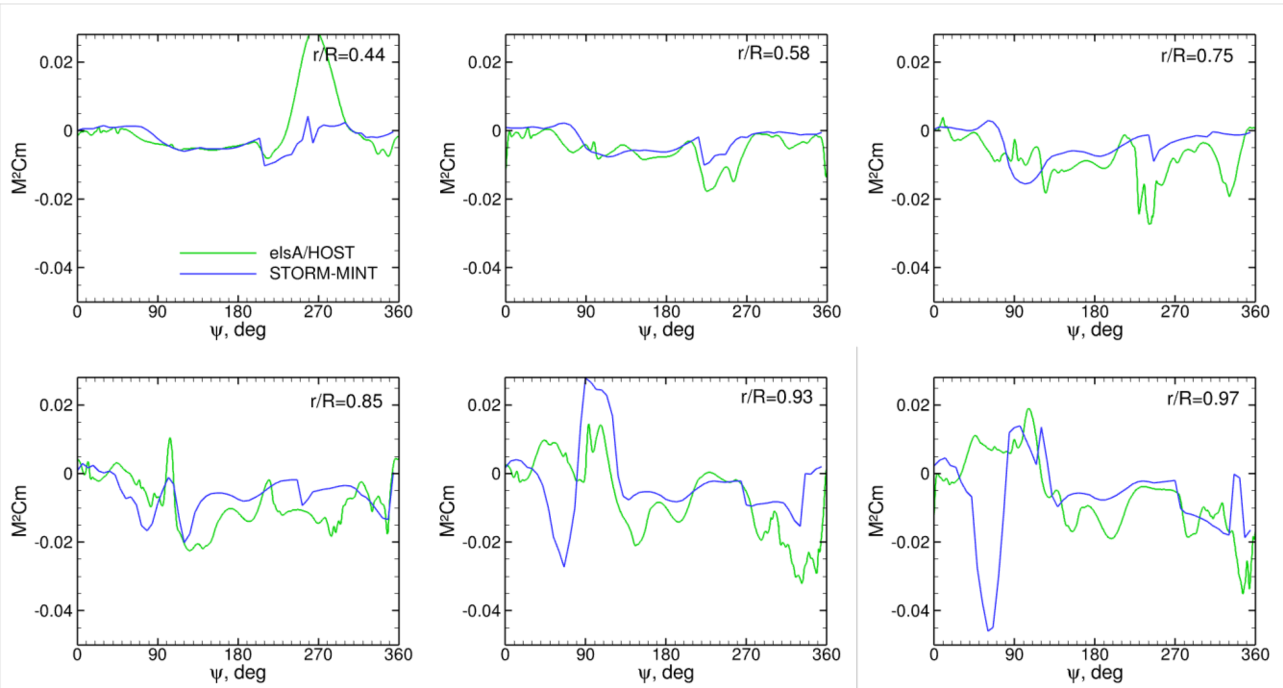

Figure 17: Section pitching moment coefficient at $\mu = 0.55$ and $\theta_0 = 7°$ (MINT: $C_T/\sigma = 0.0815$, elsA: $C_T/\sigma = 0.0902$).

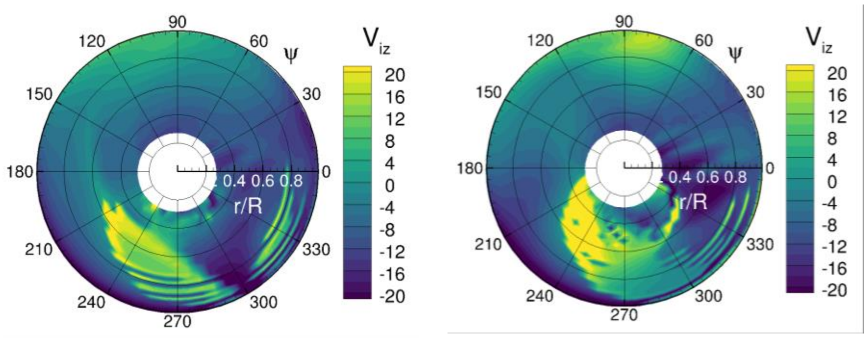

a) $\mu = 0.35$ and $\theta_0 = 5°$

b) $\mu = 0.55$ and $\theta_0 = 6°$

Figure 18: Rotor map of vertical induced velocity, negative downwash (STORM/MINT).

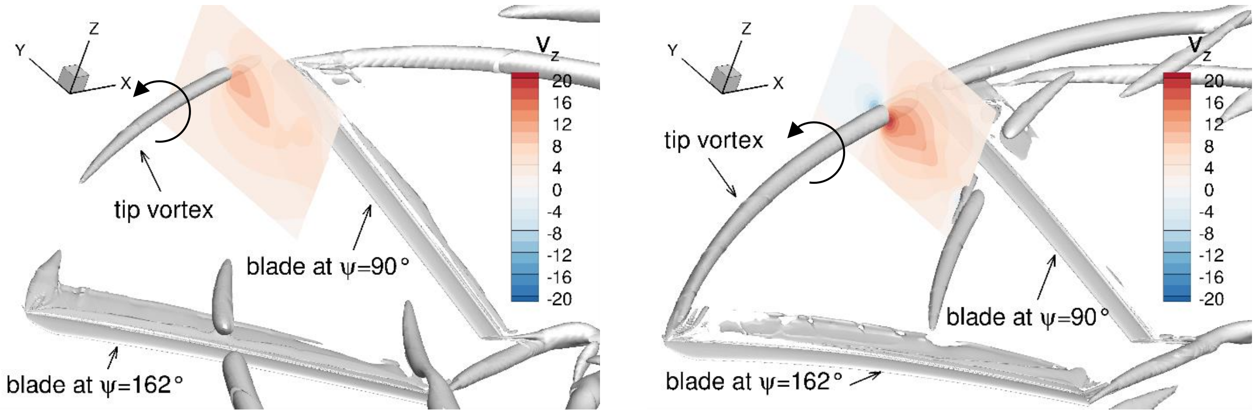

a) $\mu = 0.35$ and $\theta_0 = 5°$

b) $\mu = 0.55$ and $\theta_0 = 6°$

Figure 19: Vertical fluid velocity induced by the tip vortex just in front of the advancing blade.

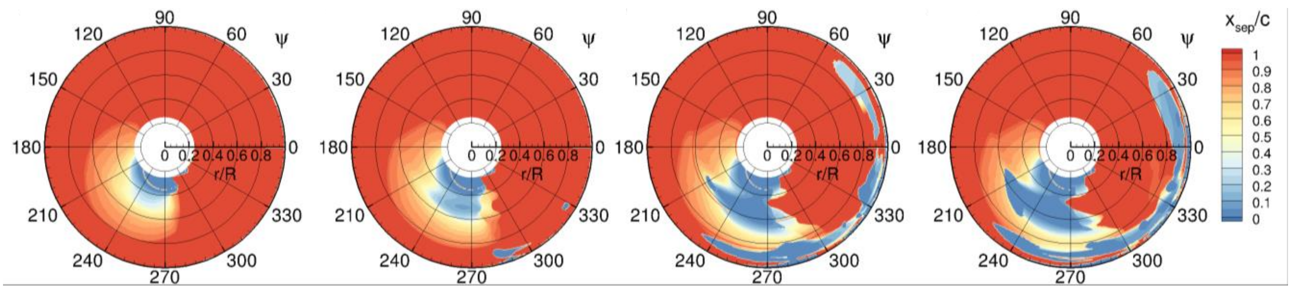

a) $\theta_0 = 1°$, $C_T/\sigma = 0.0840$

b) $\theta_0 = 4°$, $C_T/\sigma = 0.1026$

c) $\theta_0 = 5°$, $C_T/\sigma = 0.1062$

d) $\theta_0 = 6°$, $C_T/\sigma = 0.1089$

Figure 20: Rotor map of chordwise position of flow separation at $\mu = 0.35$ (elsA/HOST).

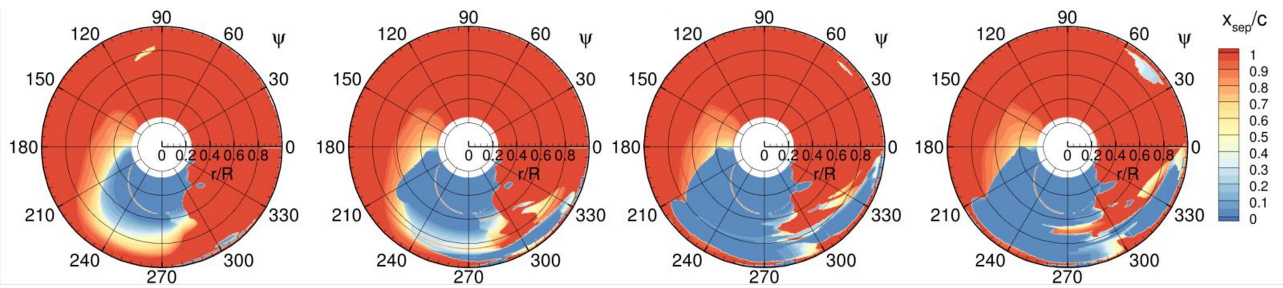

a) $\theta_0 = 2°$, $C_T/\sigma = 0.0594$

b) $\theta_0 = 4°$, $C_T/\sigma = 0.0689$

c) $\theta_0 = 6°$, $C_T/\sigma = 0.0774$

a) $\theta_0 = 7°$, $C_T/\sigma = 0.0815$

Figure 21: Rotor map of chordwise position of flow separation at $\mu = 0.55$ (elsA/HOST).

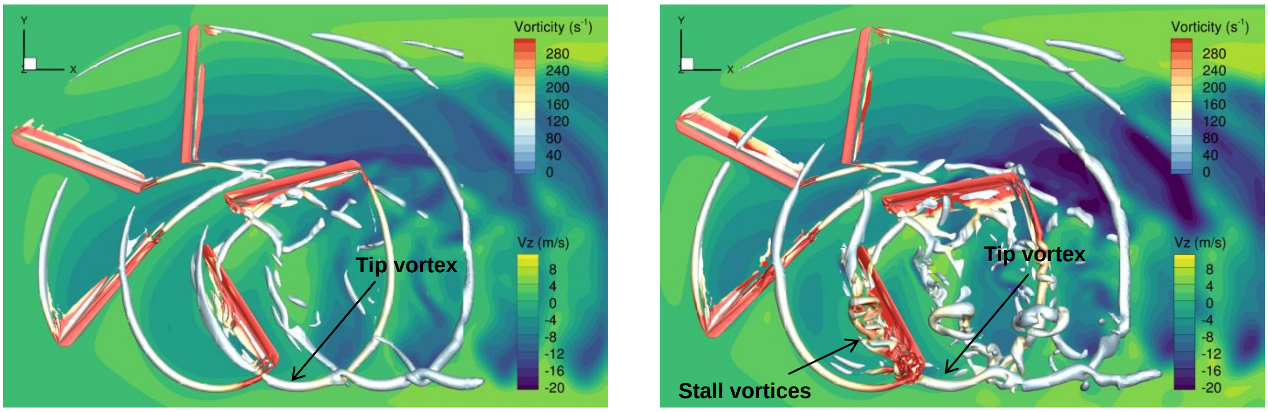

a) $\theta_0 = 1°$, $C_T/\sigma = 0.0922$ b) $\theta_0 = 5°$, $C_T/\sigma = 0.1189$

Figure 22: Iso-contour of Q-criterion colored by the vorticity and distribution of vertical fluid velocity one chord below the rotor at $\mu = 0.35$.

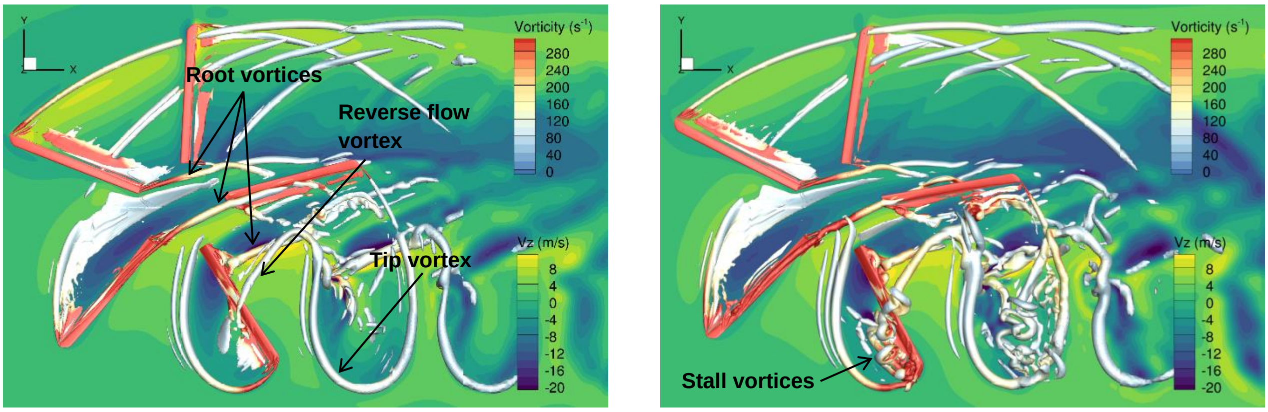

a) $\theta_0 = 2°$, $C_T/\sigma = 0.0618$ b) $\theta_0 = 6°$, $C_T/\sigma = 0.0862$

Figure 23: Iso-contour of Q-criterion colored by the vorticity and distribution of vertical fluid velocity one chord below the rotor at $\mu = 0.55$.

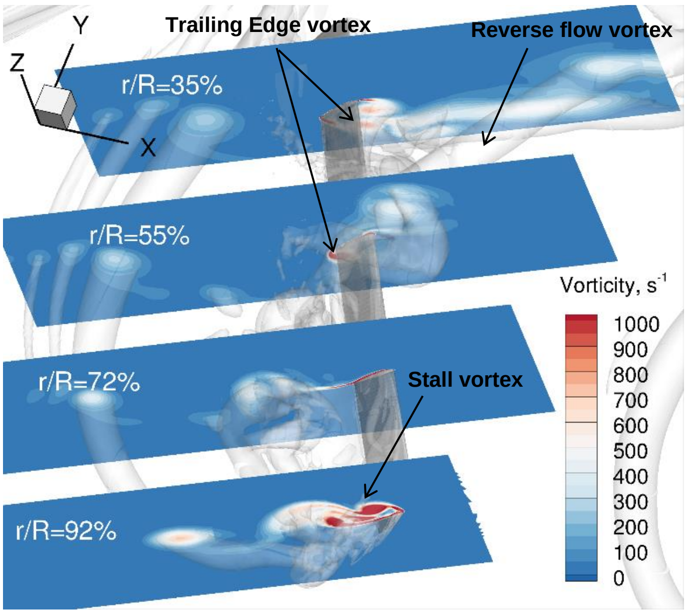

Figure 24: Vorticity magnitude at several radial slices along the retreating blade ($\psi = 306°$) at $\mu = 0.55$ and $\theta_0 = 6°$ ($C_T/\sigma = 0.0862$).

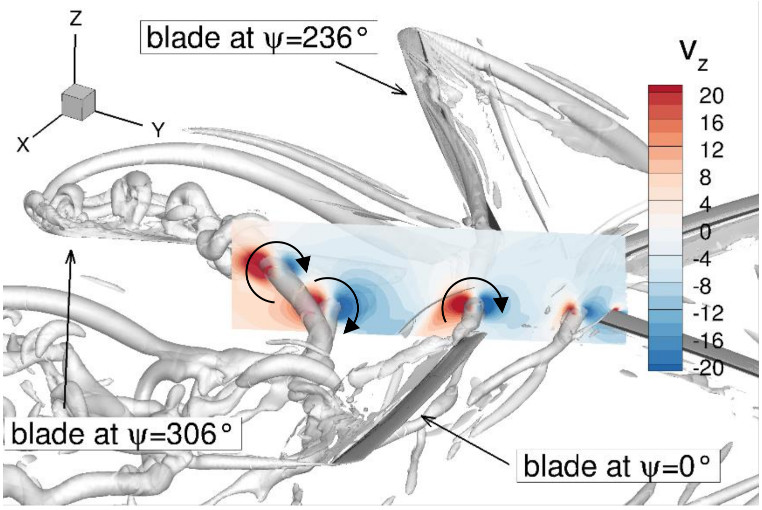

Figure 25: Fluid vertical velocity (positive upwash) on a root section of the rear blade ($\psi = 0°$) at at $\mu = 0.55$ and $\theta_0 = 6°$ ($C_T/\sigma = 0.0862$).